Featured in Physics

Opposite Effects of the Rotational and Translational Energy on the Rates of Ion-Molecule Reactions near 0 K: The $D_2^+ + NH_3$ and $D_2^+ + ND_3$ Reactions

Raphaël Hahn,[1,2] David Schlander,[1] Valentina Zhelyazkova,[1,2] and Frédéric Merkt[1,2,3,*]

[1]*Department of Chemistry and Applied Biosciences, ETH Zurich, CH-8093 Zurich, Switzerland*
[2]*Quantum Center, ETH Zurich, CH-8093 Zurich, Switzerland*
[3]*Department of Physics, ETH Zurich, CH-8093 Zurich, Switzerland*

(Received 17 October 2023; revised 20 December 2023; accepted 12 January 2024; published 1 March 2024)

The ion-molecule reactions $D_2^+ + NH_3$ and $D_2^+ + ND_3$ are studied at low collision energies (E_{coll} from zero to approximately $k_B \times 50$ K), with the D_2^+ ions in the ground rovibrational state and for different rotational temperatures of the ammonia molecules, using the Rydberg-Stark merged-beam approach. Two different rotational temperatures (approximately 15 K and approximately 40 K), measured by $(2+1)$ resonance-enhanced multiphoton-ionization spectroscopy, are obtained by using a seeded supersonic expansion in He and a pure ammonia expansion, respectively. The experimental data reveal a strong enhancement of the rate coefficients at the lowest collision energies caused by the charge-dipole interaction. Calculations based on a rotationally adiabatic capture model accurately reproduce the observed kinetic-energy dependence of the rate coefficients. The rate coefficients increase with increasing rotational temperature of the ammonia molecules, which contradicts the expectation that rotational excitation should average the dipoles out. Moreover, these reactions exhibit a pronounced inverse kinetic isotope effect. The difference is caused by nuclear-spin-statistical factors and the smaller rotational constants and tunneling splittings in ND_3.

DOI: 10.1103/PhysRevX.14.011034

Subject Areas: Atomic and Molecular Physics, Chemical Physics

I. INTRODUCTION

Understanding how the rates of chemical reactions depend on the quantum states of the reactants and on the collision energy is one of the fundamental goals of chemical physics [1,2]. Particularly strong effects are expected for ion-molecule reactions at low temperatures, because long-range electrostatic interactions lead to strongly state-specific anisotropic potentials and to a large collision-energy dependence of the reaction rates [3,4]. Recent progress in the control of the motion and quantum states of molecular ions makes it possible to investigate ion-molecule reactions with unprecedented details [5–9]. In the present article, we report on measurements of the fundamentally important reaction between state-selected molecular-hydrogen ions and ammonia near 0 K which reveal, for the first time, remarkably strong effects of the collision energy, the rotational temperature, and isotopic substitution.

Exothermic, barrier-free ion-molecule reactions are the dominant chemical processes in cold dilute environments and play a key role in astrophysics and plasma physics [10–14]. Most of the ion-molecule reaction rates (and their branching ratios) required for the modeling of the chemical composition of the interstellar medium (ISM) and planetary atmospheres have not been measured or have been measured at room temperature [15,16]. Low-temperature rate coefficients and branching ratios are usually extrapolated from data at $T > 200$ K to below 200 K using various models for the temperature dependence such as, for example, the Su-Chesnavitch model for polar molecules [17] in combination with the electrostatic properties of the neutral molecule (see, e.g., Ref. [18]). This extrapolation introduces uncertainties and errors in the ion and neutral concentrations predicted by global kinetic models [15]. At low temperature, the attractive electrostatic long-range interactions between ions and molecules imply large capture rate coefficients that can exceed the Langevin capture rate coefficients when the molecules have permanent dipole and quadrupole moments (see Ref. [4] and references therein). The dependence of the ion-molecule reaction rates on the vibrational and/or rotational temperature of the neutral molecule is mostly unknown but is expected to play an important role, particularly for regions of the ISM deviating from local thermodynamic equilibrium [19].

*Corresponding author: frederic.merkt@phys.chem.ethz.ch

Measurements of rate coefficients below 100 K are challenging, and, consequently, fewer data are available in this range than at higher temperatures. The main reason for the lack of experimental data at low collision energies is the fact that even very weak stray fields accelerate the ions and significantly heat them up (an electric potential difference of 1 mV imparts a kinetic energy of $k_B \times 12$ K to the ion). Space-charge-induced repulsion and heating also severely limit the ion densities, which can become incompatible with low-temperature investigations. Finally, common methods used to produce molecular ions such as photoionization or electron-impact ionization typically lead to ion populations distributed over multiple vibrational and rotational states.

Experimental tools and methods developed to overcome these challenges and reach low-temperature conditions in the study of ion-molecule reactions include the selected-ion-flow-tube method [20,21] which enables studies down to 80 K, cold uniform supersonic flows [22–24], with which temperatures as low as approximately 10 K can be reached; buffer-gas cooling in ion traps [7,9,25–27], with which collision energies down to approximately $3 \times k_B - 5 \times k_B$ K are accessible; laser-cooled ions and Coulomb crystals [5,28–30]; and superimposed traps of neutral atoms or molecules and ions [6,31], with which collision energies well below $1 \times k_B$ K are achievable, however, at the expense of tunability and general applicability.

In the present work, we report on the investigation of the reactions

$$D_2^+ + NH_3 \rightarrow D_2 + NH_3^+, \quad (1)$$

$$D_2^+ + NH_3 \rightarrow HD + NH_2D^+, \quad (2)$$

and

$$D_2^+ + ND_3 \rightarrow D_2 + NH_3^+ \quad (3)$$

with state-selected D_2^+ $(v^+ = 0, N^+ = 0)$ ions at collision energies in the range between zero and approximately $k_B \times 50$ K using the Rydberg-Stark merged-beam approach [8,32]. Our experiment detects only the charged products, and we cannot make any statement concerning the neutral fragments, i.e., whether the neutral products of reactions (1)–(3) are hydrogen molecules (D_2 or HD) or atoms (D + D or H + D). D_2^+ is used instead of H_2^+ because of the lower terminal velocity of the D_2 molecular beam, which provides easier access to zero relative velocity with the beam of ground-state molecules.

Reactions (1)–(3) are known to proceed at high rates from experiments carried out at room temperature [33,34] and have been studied theoretically at low temperatures [35,36].

With the Rydberg-Stark merged-beam approach, ion-molecule reactions are observed within the orbit of a highly excited Rydberg electron that shields the reaction systems from stray fields and affects neither their kinetics nor their outcome, as was demonstrated in reactions involving Rydberg states of different principal quantum number [32,37] and by verifying that the Rydberg electron is not significantly affected by the reaction [37]. This technique exploits the large dipole moments of Rydberg-Stark states (up to approximately 3400 D at $n = 30$) to deflect Rydberg-atom and -molecule beams and merge them with beams of neutral ground-state molecules. The spectator role of the electron can be understood in the realm of the independent-particle model of collisions involving Rydberg atoms and molecules [38–41].

Three main scientific questions are at the focus of this investigation. First, we examine the effect on the rate coefficients of the internal rotational excitation of the ammonia molecules, which we find to be positive. Until very recently [30], only the effects of the rotational energy of the ion have been studied experimentally [27,42,43] and found to be significant. It is, however, the rotational energy of the neutral molecules that is expected to lead to the strongest effects. In our previous study of the reaction between He^+ and ammonia [44], we did not have the possibility to measure the rotational-state population of the ammonia sample and focused on the study of the collision-energy dependence of the rate coefficients and on the kinetic isotope effect. The role of the rotational temperature of ammonia is at the center of the present study. Second, we determine the dependence of the rate coefficients on the collision energy, which we find to be negative. Finally, we clarify the origin of a surprisingly large inverse kinetic isotope effect observed in cold ion-molecule reactions involving NH_3 and ND_3 [45–49]. The opposite effect of the internal rotational energy and the translational energy on the rate coefficients was unexpected at the outset, because charge-dipole interactions average out at high rotational excitation of the neutral molecule. This apparent contradiction is interpreted using a rotationally adiabatic capture model.

II. THEORETICAL MODELING OF THE REACTION RATE COEFFICIENTS

A. The Langevin model: Shortcomings and extensions

The usual reference point for the evaluation of ion-molecule reaction rate coefficients is the Langevin model, which describes the interaction between the ion and the molecule as arising from the charge-induced-dipole interaction. The effective Langevin potential $V_{\mathrm{eff},L}(R)$ of the interaction of an ion and a neutral molecule at a distance R, including the centrifugal potential related to the collision angular-momentum $\vec{L}$, is given by [50]

$$V_{\mathrm{eff},L}(R) = -\frac{\alpha e^2}{32\pi^2\varepsilon_0^2 R^4} + \frac{\vec{L}^2}{2\mu R^2}, \quad (4)$$

where α is the polarizability of the neutral molecule, e the elementary charge, ε_0 the vacuum permittivity, and μ the

reduced mass of the collision. The model assumes that every collision with collision energy $E_{\rm coll} \geq V^{\rm max}_{{\rm eff},L}(R)$ leads to a reaction, where $V^{\rm max}_{{\rm eff},L}$ is the maximum of the L-dependent interaction potentials. This assumption results in reaction rate coefficients [51]

$$k_L = \sqrt{\frac{\alpha e^2}{4\varepsilon_0 \mu}} \tag{5}$$

that are independent of $E_{\rm coll} = \frac{1}{2}\mu v^2_{\rm rel}$ and, hence, of the asymptotic relative velocity of the reactants $v_{\rm rel}$. The Langevin model, while useful as a reference point, does not accurately describe the reaction rates of ions with dipolar molecules. The model can be extended by adding a parametrized charge-dipole interaction as, e.g., in the average-dipole-orientation [52] or in the Su-Chesnavich [17] approaches. However, these classical, semiempirical models can fail when considering cold reactants with only a few occupied quantum states [53–55], as demonstrated recently in the reactions of He^+ with CH_3F [8] and NO [56].

B. Adiabatic capture model

To describe theoretically the reaction rates of ion-molecule reactions involving dipolar and quadrupolar molecules, we implement a rotationally adiabatic capture model inspired by the pioneering works of Clary [53,54] and Troe [55] and described in detail in Refs. [8,44]. The rotational-energy-level structures in the $X\ ^1A_1'$ ground electronic state of ND_3 and NH_3 are depicted in Figs. 1(a) and 1(b), respectively. NH_3 and ND_3 are symmetric-top molecules, and their rotational states are labeled (J, K, M, p), where (J, K, M) are, respectively, the rotational-angular-momentum quantum number and the quantum numbers associated with the projections of the rotational-angular-momentum vector on the principal symmetry axis of the molecular reference frame and the z axis of the laboratory frame, typically chosen along the direction of the electric field. Their equilibrium geometry is pyramidal with a C_{3v} symmetry, leading to two potential wells separated by a barrier along the umbrella-inversion vibrational mode and quantum-mechanical tunneling between the two wells. The tunneling leads to a splitting of every (J, K) state into a doublet. The lower and upper states of the doublet are the symmetric $(p = +)$ and antisymmetric $(p = -)$ superpositions of wave functions localized in the two wells. Rotational-energy-level diagrams with full (J, K, M, p) labels and nuclear-spin-statistical factors can be found in Refs. [44,57]. ND_3 has a smaller rotational constant and, thus, a higher density of states than NH_3. Moreover, the states $(0, 0, 0, +)$, $(1, 0, M, -)$, $(2, 0, M, +)$, $(3, 0, M, -)$, etc., are not populated in NH_3 because of restrictions imposed by the Pauli principle.

To calculate state-specific rate coefficients, we implement the rotationally adiabatic capture model in the same way as for the $He^+ + NH_3$ (ND_3) reactions in Ref. [44],

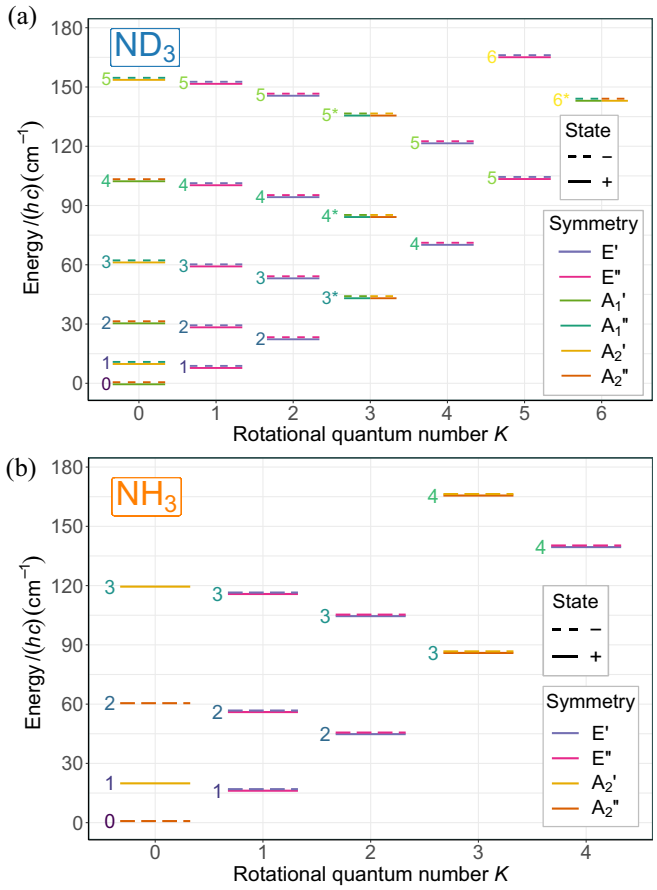

FIG. 1. Rotational level structure of ND_3 (a) and NH_3 (b) in their $X\ ^1A_1'$ ground electronic state. The rovibronic symmetry of the (J, K, p) states in the D_{3h} molecular-symmetry group and the value of p and J are indicated by the line color, the line type, and the number on the left of the lines, respectively. In (a), asterisks indicate degenerate states of different symmetry. The tunneling splittings in ND_3 are expanded by a factor of 20 for clarity.

where more details can be found. State-specific potentials $V_i(R)$ are obtained by adding the Stark shifts $\Delta E^{\rm Stark}_{J,K,M,p}(R) = \Delta E^{\rm Stark}_i(R)$ of the rotational levels in the field of the ion to the Langevin potential $V_{{\rm eff},L}(R)$:

$$V_i(R) = V_{{\rm eff},L}(R) + \Delta E^{\rm Stark}_i(R). \tag{6}$$

For each of these potentials and for a given collision energy $E_{\rm coll}$, we calculate the maximum collision angular momentum $L_{i,\rm max}$ that leads to the capture of the neutral molecule in the field of the ion. The state-specific and collision-energy-dependent capture rates $k_i(E_{\rm coll})$ are then given by [44]

$$k_i(E_{\rm coll}) = \frac{\pi L^2_{i,\rm max}}{\sqrt{2\mu^3 E_{\rm coll}}}. \tag{7}$$

The procedure is illustrated in Fig. 2, which depicts the Stark shifts of the lowest rotational levels of NH_3 and ND_3 in Figs. 2(a) and 2(d), respectively. Figures 2(b) and 2(e) show

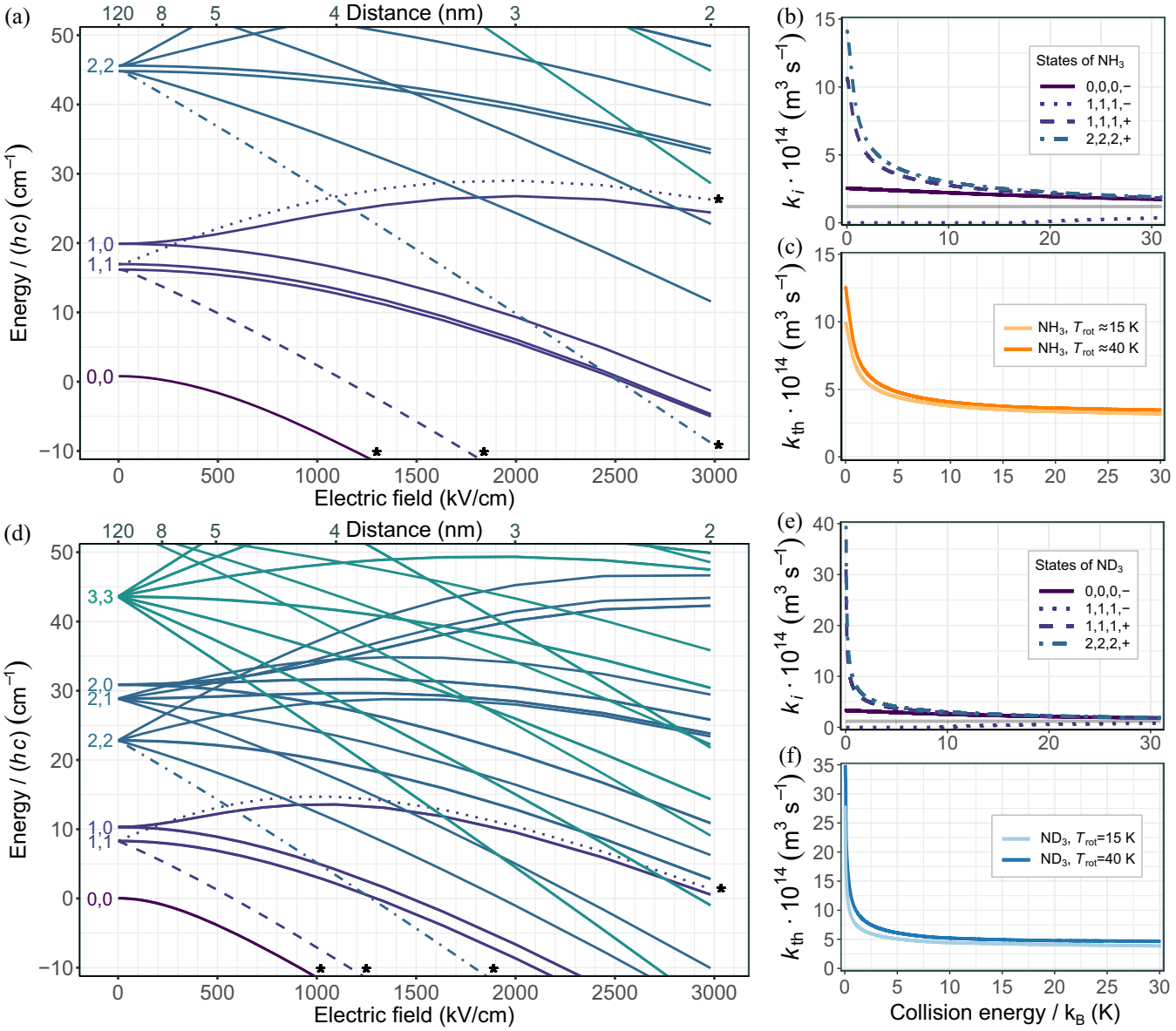

FIG. 2. Rotationally adiabatic capture model for NH_3 (a)–(c) and ND_3 (d)–(f). (a) Stark map of the rotational levels of NH_3 in the electric field of a pointlike ion at a given distance (top axis). The rotational states are labeled on the left by their quantum numbers (J, K). (b) State-specific reaction rate coefficients of the four states labeled with an asterisk in (a): $J = 0$, $K = 0$, $|M| = 0$, $p = -$ (solid, dark purple line); $J = 1$, $K = 1$, $|M| = 1$, $p = +$ (dashed, indigo line); $J = 1$, $K = 1$, $|M| = 1$, $p = -$ (dotted, indigo line); and $J = 2$, $K = 2$, $|M| = 2$, $p = +$ (dash-dotted, teal line). The Langevin rate coefficient is indicated by the gray horizontal line. (c) Averaged reaction rate coefficients $k_{th}(E_{coll}, T_{rot})$ obtained using the calculated state-specific rate coefficients and the measured occupation probabilities of the rotational states for an expansion of pure NH_3 ($T_{rot} \approx 40$ K) (dark orange line) and a seeded expansion (5%) in He ($T_{rot} \approx 15$ K) (light orange line). (d)–(f) The same as (a)–(c) but for ND_3.

the calculated state-specific capture rate coefficients for the four states $(0, 0, 0, -)$ (solid, dark purple line), $(1, 1, 1, +)$ (indigo, dashed line), $(1, 1, 1, -)$ (indigo, dotted line), and $(2, 2, 2, +)$ (teal, dash-dotted line) of NH_3 and ND_3, respectively. States with negative Stark shifts show an increase of the capture rate coefficients as the collision energy decreases below 20 K, whereas the capture rate coefficients of the states with positive Stark shifts typically vanish below 10 K. At high collision energies, the state-specific rate coefficients tend toward the Langevin rate coefficient (in gray). The theoretical capture rate coefficient

$$k_{th}(E_{coll}, T_{rot}) = \sum_i P_{i,T_{rot}} k_i(E_{coll}) \tag{8}$$

for a given rotational temperature T_{rot} of the ammonia sample is obtained by multiplying these state-specific rates with the corresponding rotational-state occupation

probabilities $P_{i,T_{\rm rot}}$. In the present work, we measure these probabilities using $(2+1)$ resonance-enhanced multiphoton-ionization (REMPI) spectroscopy. The values of $k_{\rm th}$ for experimentally determined rotational-state occupation probabilities of NH_3 and ND_3 (corresponding to rotational temperatures of 15 and 40 K, respectively) are displayed in Figs. 2(c) and 2(f), respectively. The values compare favorably with the estimated reaction rate coefficient for $H_2^+ + NH_3$ at 10 K available in the kinetic database for astrochemistry of 2.57×10^{-8} cm^3 s^{-1} [18]. The version of capture theory employed here treats the motion over the barrier as purely classical, which is likely to be valid for the collision-energy range considered here.

III. EXPERIMENTAL METHODS

A. Merged-beam experimental setup

The experimental setup and procedure are described in Ref. [58], and only the main aspects and the relevant modifications are presented in this section. A schematic view of the setup is shown in Fig. 3. The reactions are studied using supersonic molecular beams produced by two homemade pulsed valves producing short (approximately 20 μs) pulses of gas at a repetition rate of 25 Hz. NH_3 and ND_3 are used either pure or in a (5:95) mixture with He. Helium is chosen as the carrier gas to inhibit the formation of ammonia clusters [59] and to increase the mean velocity of the beam. Two skimmers (with diameters of 20 and 3 mm) and two pairs of razor blades constrain the size and the transverse velocity of the ammonia beam. The second beam [hereafter referred to as the $D_2(n)$ beam] is formed from a skimmed beam of D_2 molecules via resonant three-photon excitation to Rydberg-Stark states of principal quantum number $n = 29$ belonging to the Rydberg series converging to the $D_2^+(v^+ = 0, N^+ = 0)$ ionization threshold. The photoexcitation takes place between two electrodes used to generate an electric field of 10 V/cm. This electric field mixes Rydberg states of different values of the orbital-angular-momentum quantum number l, which results in Rydberg-Stark states with large dipole moments that are sensitive to electric-field gradients. The photoexcitation is carried out near the surface of an on-chip Rydberg-Stark deflector [32], with which time-dependent electric fields are applied to trap, deflect, and accelerate the Rydberg molecules. We use this Rydberg-Stark deflector to merge the $D_2(n)$ and the ammonia beams, which initially propagate along axes separated by 10°, and to set the velocity of the $D_2(n)$ molecules. For a $D_2(n)$ beam traveling initially at 1500 m/s, the final velocity v_f can be adjusted in the range between 1000 and 2100 m/s, corresponding to collision energies ranging from $E_{\rm coll}/k_B \approx 0$ K to $E_{\rm coll}/k_B \approx 50$ K (see Fig. 5 below).

The merged beams enter the reaction chamber, comprising a time-of-flight mass spectrometer in a Wiley-McLaren configuration. An adjustable slit (see Fig. 3) blocks the untrapped Rydberg molecules and prevent them from entering the reaction chamber. The positively charged reaction products and D_2^+ ions produced by field ionization of the $D_2(n)$ molecules are extracted toward a microchannel-plate (MCP) detector by applying two precisely timed electric-field pulses of different amplitudes across the reaction volume. The first, weaker pulse (prepulse) removes all ions from the reaction region and defines the beginning of the reaction-observation temporal window. The second electric-field pulse is applied when the cloud of Rydberg molecules reaches the center of the reaction region and extracts the product ions. The field-free interval between the two pulses represents the reaction-observation time τ_R and is kept constant at 14 μs for all measurements. The density of ammonia molecules is expected to be more than 3 orders of magnitude larger than that of $D_2(n)$. Moreover, the molecule densities are such that the reaction probability for a $D_2(n)$ molecule is less than 1%. Consequently, the reaction rates are well described by pseudo-zero-order kinetics. In preliminary experiments, we verified that the integrated product-ion signals are proportional to τ_R, as expected for pseudo-zero-order kinetics.

For each selected collision energy, the ion signals are averaged over typically 5000 experimental cycles by a fast digital oscilloscope. To remove the contributions from reactions of $D_2(n)$ with the background gas, time-of-flight spectra are also recorded under conditions where the pulses of $D_2(n)$ and ammonia molecules do not overlap temporally in the reaction region. These background time-of-flight spectra are then subtracted from the recorded traces. The velocity and temporal distributions of the $D_2(n)$ and ammonia beams are characterized using (see Fig. 3)

(i) two fast-ionization gauges (FG_1 and FG_2 in Fig. 3) to measure the temporal profile of the neutral beam at two different positions—from this measurement, the velocity and spatial distributions of the ammonia beam can be inferred (see Sec. III B 1);
(ii) a movable imaging MCP detector (on-axis MCP) that can be slid into the beam to record the size of the $D_2(n)$ molecular cloud and its temporal profile—in this way, the transverse and the longitudinal velocity distributions of the $D_2(n)$ beam can be precisely determined (see Sec. III B 2); and
(iii) a REMPI chamber equipped with a pair of electrodes and located beyond the reaction chamber, used to record $(2+1)$ REMPI spectra of the ammonia samples and determine their rotational temperature (see Sec. III D).

B. Beam characterization and determination of the collision energies

The collision energy $E_{\rm coll}$ in our merged-beam experiment is given by

$$E_{\rm coll} = \frac{1}{2}\mu||\vec{v}_{\rm rel}||^2 = \frac{1}{2}\mu v_{\rm rel}^2, \tag{9}$$

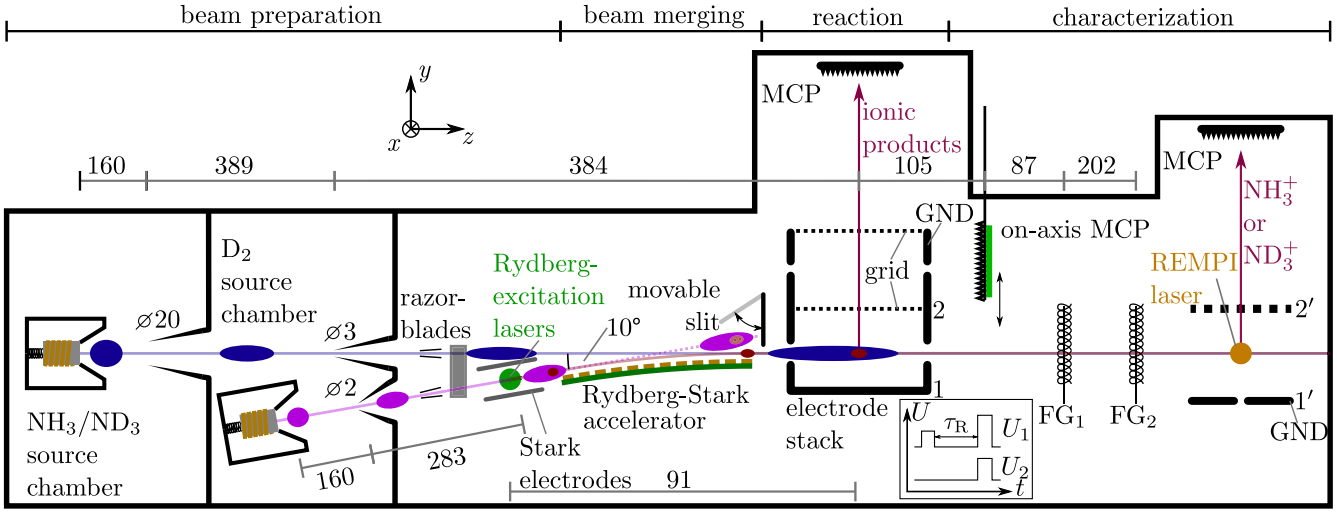

FIG. 3. Schematic view of the experimental setup (not to scale). MCP, microchannel-plate detector; FG, fast-ionization gauge; GND, ground potential. A beam of Rydberg D_2 molecules is formed by photoexcitation in a supersonic expansion of pure D_2 between two electrodes. It is merged with a beam of either pure NH_3 (ND_3) or NH_3 (ND_3) seeded in He with a 5:95 ratio using a Rydberg-Stark accelerator. Cationic products of the reaction are extracted toward an MCP detector by applying pulsed electric potentials U_1 and U_2 (see the inset) on electrodes 1 and 2, respectively, and their masses are deduced from their time of flight. A movable imaging MCP allows the characterization of the accelerated $D_2(n)$ molecules. FG_1 and FG_2 are used to measure the velocity distribution and density of the ammonia molecules. A permanent electric field is applied between electrodes 1′ and 2′ to extract photoionization products (NH_3^+ or ND_3^+) toward an MCP detector. All distances are in millimeters.

with

$$||\vec{v}_{\rm rel}|| = \sqrt{(v_{{\rm Ry},x}-v_{{\rm n},x})^2+(v_{{\rm Ry},y}-v_{{\rm n},y})^2+(v_{{\rm Ry},z}-v_{{\rm n},z})^2}. \tag{10}$$

In Eq. (10), $v_{{\rm n},x}, v_{{\rm n},y}, v_{{\rm n},z}$ and $v_{{\rm Ry},x}, v_{{\rm Ry},y}, v_{{\rm Ry},z}$ are the components of the velocity vectors of the ammonia and $D_2(n)$ molecules, respectively (see Fig. 3 for the definition of the x, y, z directions). To reliably determine the collision-energy dependence of the reaction rate coefficients, it is essential to determine the collision-energy distribution $\rho(E_{\rm coll}; v_f)$ for each selected value of the mean final longitudinal velocity v_f of the $D_2(n)$ cloud.

The determination of $\rho(E_{\rm coll}; v_f)$ thus requires knowledge of the three-dimensional relative-velocity distributions $\rho(\vec{v}_{\rm rel}; v_f)$ of the ammonia and $D_2(n)$ molecules in the reaction volume for each v_f. The quantity $\rho(\vec{v}_{\rm rel}; v_f)$ is derived from independent measurements of the three-dimensional velocity of the ammonia and $D_2(n)$ beams.

1. Characterization of the ammonia beam

The velocity distributions of the NH_3 and ND_3 beams are measured at each experimental cycle by recording the temporal profiles of the gas density using the two FGs located beyond the reaction region (see Fig. 3). The procedure we follow is illustrated by the representative dataset displayed in Fig. 4, which shows the time-of-flight distributions for a seeded expansion of NH_3 in He (5:95) recorded at the first (red) and second (blue) FG. Both distributions have the same overall shape and are wider [full width at half maximum (FWHM) of approximately 70 μs] than the 20-μs-long valve-opening time. Consequently, the observed time-of-flight distributions can be decomposed

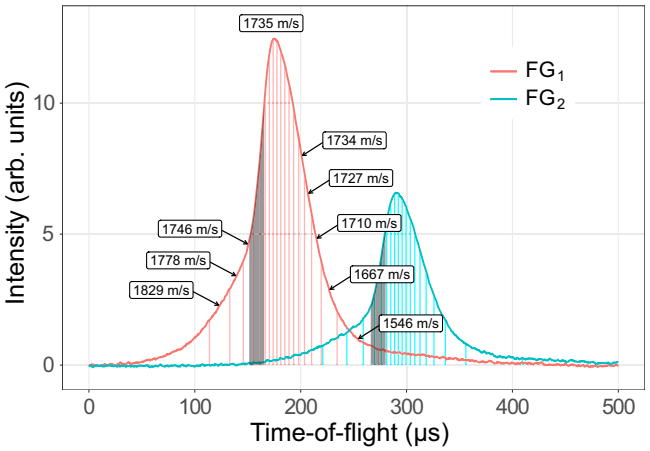

FIG. 4. Determination of the velocity $\overline{v_{{\rm n},z}}$ of the NH_3 beam seeded in He from the time-of-flight distributions recorded at the two FGs. The time-of-flight profiles are divided into 20 bins with equal areas under the curve (indicated with red and blue vertical lines for the first and second FG, respectively). The area shaded in gray on each FG profile corresponds to the molecules overlapping with the $D_2(n)$ cloud during the 14-μs-long reaction-observation temporal window. This area is used for normalization of the product-ion signal. The origin of the time-of-flight scale corresponds to the laser photoexcitation pulse.

into multiple pairs of corresponding temporal bins, indicated by the vertical lines. One such pair, representing the part of the beam that overlaps with the $D_2(n)$ cloud in the middle of the reaction region, is shaded in gray. The longitudinal velocities $v_{n,z}$ associated with the different bin pairs can be directly obtained by dividing the distance d_{FG} between the two FGs by the time-of-flight difference between the bins of each pair. The velocities given in Fig. 4 are obtained using a d_{FG} value of 20.2 cm, which was determined in a separate calibration measurement using a pure He beam. These velocities illustrate that the short valve-opening times and the long flight distance (see Fig. 3) enable a high degree of velocity selection (around 5 m/s in the present case), as already pointed out in earlier studies [60,61].

Our measurements yield a mean velocity $\overline{v_{n,z}} = 1735(3)$ m/s for the selected bin of the ammonia:He mixtures. Similar measurements for expansions of pure ammonia revealed much broader time-of-flight distributions, with Gaussian FWHM of up to 400 μs, indicating much broader distributions of velocities than for the seeded beams (see Fig. 4). Based on earlier works reporting similar observations [62–64], we attribute this behavior to the formation of clusters in the expansion and the resulting heating of the expanding gas through the release of approximately 170 meV of energy per clustering ammonia molecule [65]. In such expansions, the fastest molecules at the front of the gas pulse are primarily monomers. To avoid clusters in our measurements involving pure ammonia expansions, we select velocity bins around $\overline{v_{n,z}} = 1380(3)$ m/s for NH_3 and $\overline{v_{n,z}} = 1330(3)$ m/s for ND_3, which are faster than the mean beam velocities of 1080 and 1050 m/s, respectively.

The shot-to-shot characterization of the velocity distribution of the ammonia beam with the two FGs is a crucial element of our procedure. Slow drifts of the gas-expansion conditions, resulting from temperature variations of the valve, are automatically accounted for in the analysis. Moreover, the known distance from the FGs to the middle of the reaction zone enables us to accurately set the longitudinal velocity $\overline{v_{n,z}}$ of the ammonia molecules that overlap with the $D_2(n)$ cloud by adjusting the ammonia valve-opening trigger time. Finally, the high degree of transverse-velocity selection through the skimmers and the two pairs of razor blades implies that (i) $\overline{v_n} \approx \overline{v_{n,z}}$ and (ii) the distribution of collision energies is entirely determined by the much broader velocity distribution of the $D_2(n)$ beam (see below). Consequently, for each collision, the relative velocity is given by the velocity of the $D_2(n)$ molecule:

$$|v_{rel}| \approx \sqrt{v_{Ry,x}^2 + v_{Ry,y}^2 + (v_{Ry,z} - \overline{v_n})^2}. \quad (11)$$

2. Characterization of the $D_2(n)$ beam

To determine the transverse and the longitudinal velocity distributions for each selected $D_2(n)$-beam mean velocity v_f, we combine images of the $D_2(n)$-molecule cloud recorded using the on-axis movable MCP and particle-trajectory simulations of the trapping and deflection procedure. The images are recorded in separate experiments carried out just before or after recording the corresponding product-ion time-of-flight spectra. A two-dimensional Gaussian function is used to fit the images, with different widths for the x and y directions. The mean velocities along x and y are determined by comparing the width of the $D_2(n)$-molecule cloud at the end of the deflector (obtained in the numerical particle-trajectory simulations) and the width at the position of the MCP extracted from the images. The mean transverse velocities ($\overline{v_{Ry,x}}$, $\overline{v_{Ry,y}}$) are always found to be between 10 and 30 m/s, with $\overline{v_{Ry,y}}$ typically twice as large as $\overline{v_{Ry,x}}$. In these imaging experiments, we also verify that the size of the $D_2(n)$-molecule cloud does not exceed the size of the ammonia beam, because this would lead to an undesired loss of product-ion signal. For v_f values below 1100 m/s, we observe a significant increase of the $D_2(n)$-molecule cloud size, and the corresponding data are not included in the analysis.

The velocity distribution of the $D_2(n)$-molecule cloud along the z direction is determined using (i) the measured time-of-flight distribution on the on-axis MCP, (ii) the time at which the $D_2(n)$-molecule cloud is in the center of the reaction chamber, as determined by pulsed-field ionization, and (iii) the known distance between the center of the chamber and the on-axis MCP (see Fig. 3). The time-of-flight traces are very well reproduced by Gaussian distributions. Their FWHM are around 20 m/s and depend only slightly on v_f. The mean values of these distributions $\overline{v_{Ry,z}}$ slightly deviate from the v_f values programmed on the deflector because of imperfect acceleration over the chip. The deviations increase with the magnitude of the acceleration.

Figure 5 depicts the distributions of collision-energy probability densities $\rho(E_{coll}; v_f)$ for different values of the mean velocity of the $D_2(n)$-molecule beam and for a mean velocity $\overline{v_{n,z}} = 1735$ m/s of the supersonic beam of NH_3 seeded in He. The inset shows the distributions at low collision energies on an enlarged scale and demonstrates that the collision-energy resolution is better than $k_B \times 500$ mK at the lowest collision energies.

C. Determination of the collision-energy-dependent reaction rate coefficients

The product-ion signals $I_i(v_f)(i = NH_3^+, NH_2D^+$ for the $D_2^+ + NH_3$ reaction) observed at a given final velocity v_f of the $D_2(n)$ beam,

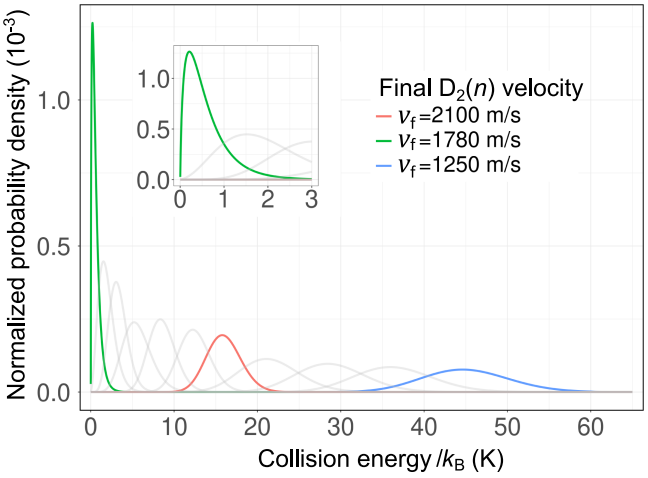

FIG. 5. Total-collision-energy probability density $\rho(E_{\rm coll}; v_f)$ determined for the $D_2(n) + NH_3$ reaction after merging a beam of NH_3 seeded in He (5:95) with mean velocity $\overline{v_{n,z}} = 1735(3)$ m/s with a beam of $D_2(n)$ molecules with mean longitudinal velocities between 1250 and 2100 m/s. $\rho(E_{\rm coll}; v_f =$ 2100 m/s), $\rho(E_{\rm coll}; v_f = 1780$ m/s), and $\rho(E_{\rm coll}; v_f = 1250$ m/s) are displayed in red, green, and blue, respectively. See the text for details.

$$I_i(v_f) \propto \tau_R k_{\rm exp}(v_f)[NH_3][D_2(n)], \tag{12}$$

are proportional to τ_R, to the densities $[NH_3]$ and $[D_2(n)]$ in the region where both beams overlap, and to an effective rate coefficient

$$k_{\rm exp}(v_f) = \int_{E_{\rm coll}} k_{\rm th}(E_{\rm coll})\rho(E_{\rm coll}; v_f)\mathrm{d}E_{\rm coll}, \tag{13}$$

where $\rho(E_{\rm coll}; v_f)$ is determined from experimental data as explained in Sec. III B 2 and $E_{\rm coll}$ is given by Eqs. (9) and (11). To remove the influence of $[NH_3]$ and $[D_2(n)]$, we normalize the measured signal for each v_f value with quantities proportional to $[NH_3]$ and $[D_2(n)]$. In the case of $[NH_3]$ (and $[ND_3]$), we use the time-of-flight profiles measured at the FGs (see gray shaded areas in Fig. 4). In the case of $[D_2(n)]$, we use the strength of the D_2^+-ion signal generated by the pulsed-field ionization when the ion-extraction pulse is applied. The amplitude of this pulse (approximately 30 V/cm) is not large enough to efficiently field ionize the initially prepared $n = 29$ Rydberg states (their field-ionization threshold is 454 V/cm). Consequently, the detected D_2^+ ion signal originates from a small fraction of the $D_2(n)$ molecules that have undergone transitions to higher Rydberg states by absorption of thermal radiation or collisions during their flight from the decelerator to the reaction region. When determining $k_{\rm exp}$ from the measured product signal, one must correct for the fact that the D_2^+ signal increases with increasing $D_2(n)$ flight time and, thus, decreases with increasing v_f values. For instance, the D_2^+ signal obtained at the largest v_f value (2000 m/s) is 30% smaller than that obtained for the slowest v_f value (1250 m/s), although the number of $D_2(n)$ molecules is the same in both cases.

D. Determination of the rotational temperature of the ammonia sample via (2 + 1) REMPI spectroscopy

The rotational temperatures of the NH_3 and ND_3 samples are determined by (2 + 1) REMPI spectroscopy of selected bands of the $B' \leftarrow X$ and $C' \leftarrow X$ electronic transitions around 313 nm [66]. The pulsed laser radiation is generated by frequency doubling the output of a Nd:YAG-pumped dye laser (operated with DCM dye) in a β-barium-borate crystal. The laser wave number is measured with a wave meter, and the laser intensity is monitored by a fast photodiode. The laser beam crosses the merged beam at right angles in the REMPI chamber beyond the reaction region (see Fig. 3), and the NH_3^+ or ND_3^+ ions are extracted toward an MCP detector in a direction (y) perpendicular to the merged beam. To obtain reliable intensity distributions, the spectra are recorded at low enough laser intensities I so that the (2 + 1) REMPI process is not saturated, and the ionization signal is proportional to I^3. The ion signal is then normalized by dividing through I^3.

The rotational temperature is obtained by comparing the experimental intensity distributions with intensity distributions calculated using the program PGOPHER [67] and molecular constants from Refs. [68–71]. The procedure is illustrated in Figs. 6(a) and 6(b), where spectra for a seeded and a pure ND_3 sample are compared, respectively. In these figures, the normalized experimental intensity distributions are compared with intensity distributions calculated for rotational temperatures $T_{\rm rot}$ of 15 and 40 K, respectively. Figures 6(e) and 6(f) depict the rotational-state occupation probabilities at these temperatures, which are used to compute $k_{\rm th}$ [see Eq. (8)].

The same procedure for the NH_3 sample is illustrated in Figs. 6(c), 6(d), 6(g), and 6(h). In the case of NH_3, significant deviations from a Maxwell-Boltzmann rotational-state population distribution are observed. This nonthermal behavior was already observed for NH_3 in Refs. [72–74]. However, the $T_{\rm rot}$ value that is closest to the observed distribution in NH_3 is the same as for the pure ND_3 and for the seeded ND_3 samples. To determine $k_{\rm th}$ in this case, we use the actually observed occupation probabilities, as reported in Figs. 6(g) and 6(h).

IV. RESULTS AND DISCUSSION

A. Branching ratio of the $D_2^+ + NH_3(ND_3)$ reaction

Figure 7 compares the time-of-flight spectrum obtained for the reaction $D_2(n) + NH_3$ at a collision energy of $k_B \times 500$ mK (green line) with a background spectrum (light purple line) recorded after delaying the NH_3 pulse so that the NH_3 and $D_2(n)$ gas pulses did not overlap in the

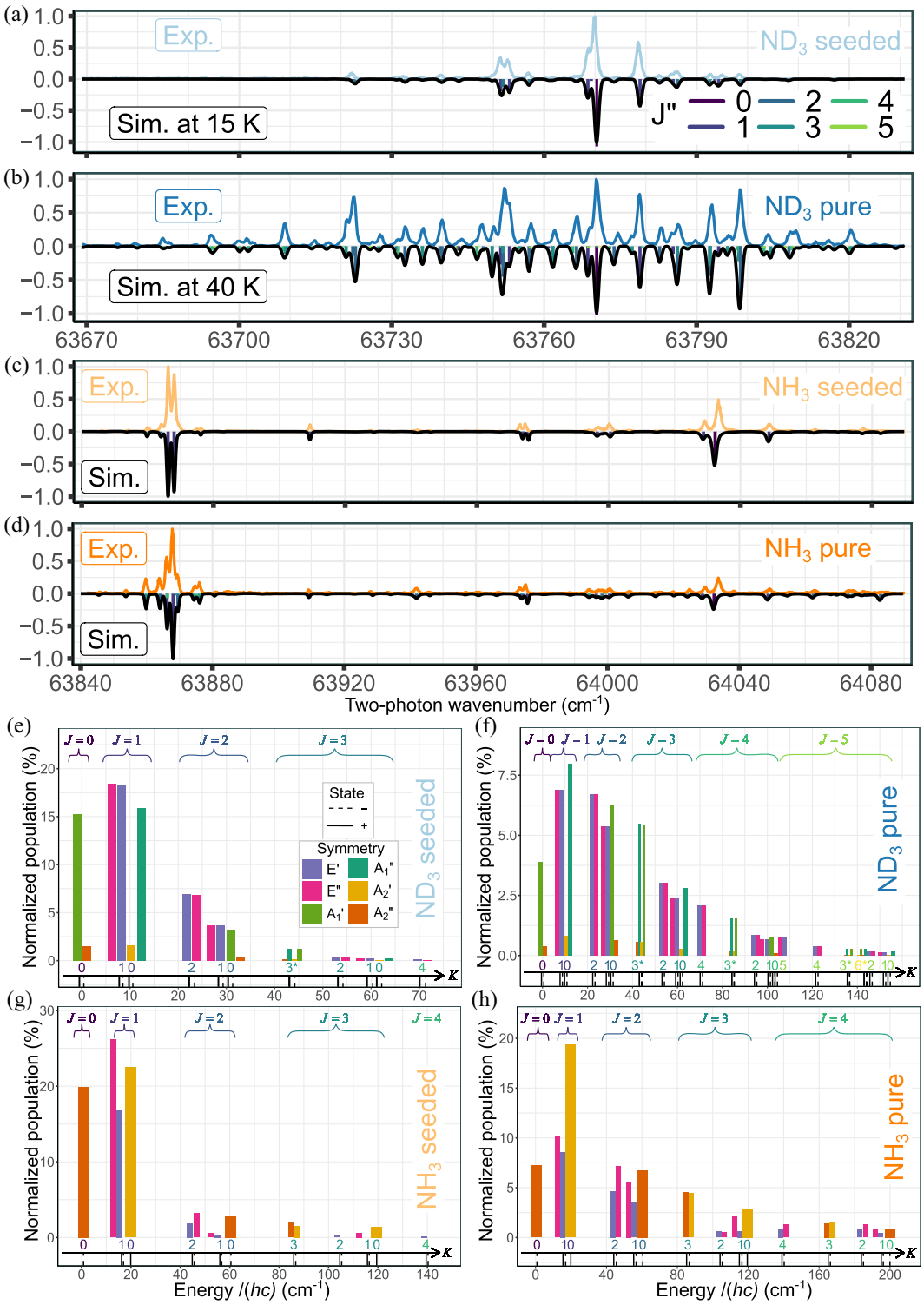

FIG. 6. (a) [(b)] Normalized (2 + 1) REMPI spectrum (y axis in arbitrary units) (top, experimental; bottom, inverted, simulated) of the seeded [pure] ND_3 sample, showing the transitions to the $B'(v = 6)$ states. The colors of the vertical bars in the simulated spectrum indicate the rotational quantum number J'' of the initial state. (c) [(d)] The same as (a) [(b)] for NH_3 for the transitions to the $B'(v = 5)$ and $C'(v = 0)$ states. (e)–(h) Rotational-state occupation probabilities for the seeded ND_3, pure ND_3, seeded NH_3, and pure NH_3 samples, respectively. The tunneling doublet is indicated as in Fig. 1, and the splitting is multiplied by a factor of 20 for ND_3, for clarity. K quantum numbers are indicated below the vertical bars.

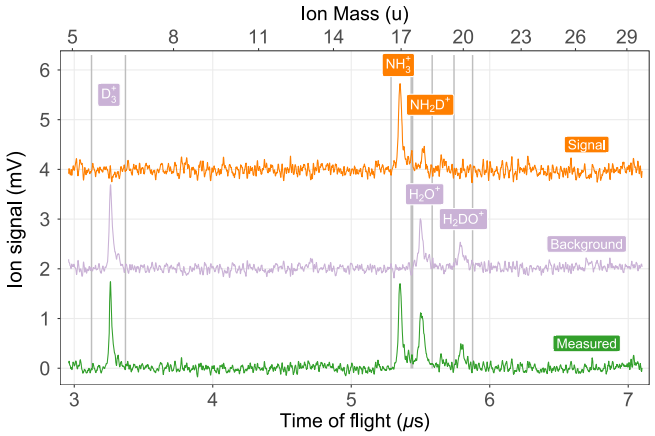

FIG. 7. Experimental time-of-flight traces showing the ionic products of the reaction of $D_2(n)$ with NH_3. The product signals NH_3^+ and NH_2D^+ (in orange) are obtained from the green time-of-flight trace after subtraction of the background signal (purple) and integration over the temporal windows marked by the vertical lines. Offsets of 2 and 4 mV are, respectively, added to the background and signal traces for clarity.

reaction zone. The latter spectrum consists of contributions from D_3^+, H_2O^+, and H_2DO^+ originating from the reactions of $D_2(n)$ with D_2 and H_2O molecules in the reaction-chamber background gas. After removing these contributions by subtraction, we obtain the time-of-flight spectrum displayed in orange, which consists of a dominant NH_3^+ (from the charge-transfer reaction $D_2^+ + NH_3 \rightarrow NH_3^+ + D_2$) and a weaker NH_2D^+ signal (from the reaction $D_2^+ + NH_3 \rightarrow NH_2D^+ + HD$). The relative intensities of 5:1 of these two product channels are found not to depend on the collision energy in the range from 0 to $k_B \times 50$ K and are compatible with the earlier observations of Kim and Huntress [34], who reported that 78% (22%) of the reactions yield $NH_3^+ + D_2$ ($NH_2D^+ + HD$). In the case of the $D_2^+ + ND_3$ reaction, the two product channels cannot be distinguished by time-of-flight mass spectrometry.

B. Comparison of experimental and theoretical rate coefficients

Figures 8(a) and 8(c) show how the measured product-ion signals (dots with vertical error bars representing one standard deviation), normalized by the $D_2(n)$ and ammonia densities, vary with the nominal relative velocity $\overline{v_{\mathrm{Ry},z}} - \overline{v_{\mathrm{n}}}$ of the $D_2(n)$ and ammonia beams, determined as explained in Sec. III. The data presented in Fig. 8(a) correspond to experiments carried out with seeded beams of NH_3 and ND_3 and a rotational temperature of approximately 15 K. Those displayed in Fig. 8(c) are obtained with beams of pure NH_3 and ND_3 and a rotational temperature of approximately 40 K. In the experiments, we do not measure absolute NH_3, ND_3, and $D_2(n)$ particle densities but only relative densities. By normalizing the product-ion signals by the measured relative densities, we can nevertheless reliably determine the dependence of the rate coefficients on the relative velocity and the collision-energy [see Eq. (12)]. Figures 8(b) and 8(d) display the same data as Figs. 8(a) and 8(c) as a function of the nominal collision energy $\frac{1}{2}\mu(\overline{v_{\mathrm{Ry},z}} - \overline{v_{\mathrm{n}}})^2$ and multiplied by a scaling factor (one per dataset) to best reproduce the calculated averaged capture rate coefficients. Using a global scaling factor relies on the assumption that the capture probability is constant over the investigated range of collision energies, which is justified for the relatively small range under consideration.

The full lines in Fig. 8 represent the results of the calculations of the rate coefficients taking into account the distributions of relative collision energies and the populations of the rotational levels of NH_3 and ND_3 determined experimentally [see Secs. III B and III D, in particular, Eq. (13)]. The calculated and experimental data in Fig. 8 agree within the experimental uncertainty. Given that no adjustable parameters are used beyond the global scaling factors for the product-ion signals, this agreement indicates that the rotationally adiabatic capture model adequately describes the collision-energy-dependent rate coefficients over the range of conditions probed in our experiments. This agreement, in turn, makes it possible to compare experimental data acquired under different conditions and draw conclusions concerning the origin of the observed trends.

C. Influence of the collision energy

Figure 8 reveals that in all cases, i.e., for the reactions involving both NH_3 and ND_3 at both rotational temperatures, the product-ion signal increases with decreasing collision energy. This increase can be interpreted within the rotationally adiabatic capture model as arising from the Stark shifts of the rotational levels of NH_3 and ND_3 in the field of the D_2^+ ion. The rate coefficients of states with negative Stark shifts increase much faster with decreasing collision energies than the rate coefficients of states with positive Stark shift decrease (see Fig. 2). This effect is general and characteristic of polar molecules. In the case of ammonia, it is enhanced by the fact that the rotational levels occur as tunneling doublets of opposite parity that are coupled by even weak electric fields.

D. Influence of the rotational temperature

Comparison of Figs. 8(b) and 8(d) enables the analysis of the effects of the increase of the rotational temperature of the ammonia samples from 15 to 40 K. The main effect is an overall increase of the reaction rate coefficient over the full range of values of E_{coll} investigated experimentally. A second effect is a steeper increase of the rate coefficient at the lowest collision energies (below 5 K) for the $T_{\mathrm{rot}} =$ 40 K samples. The increase of the reaction rate coefficients with increasing rotational temperature is surprising at first

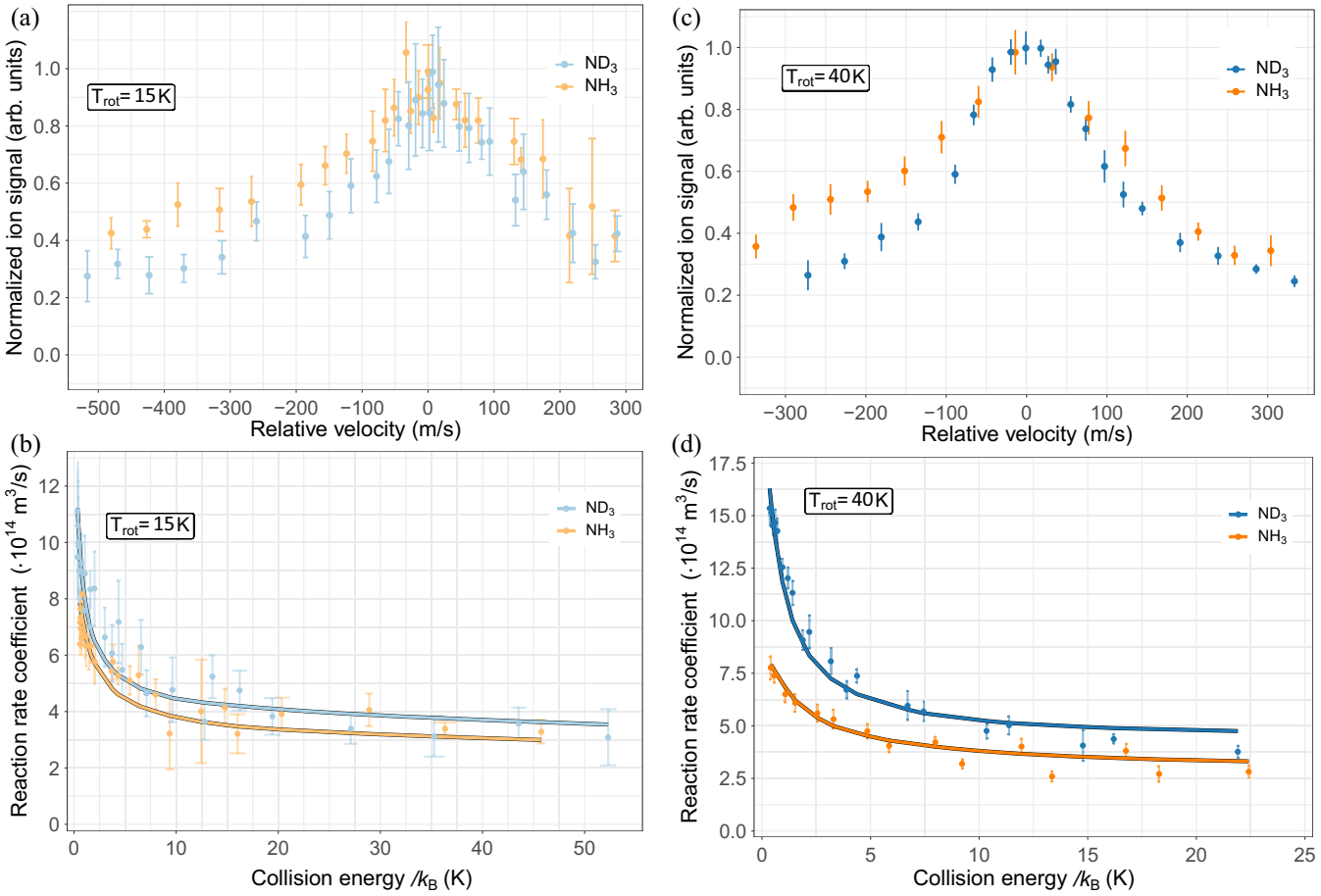

FIG. 8. Product-ion signals of the $D_2^+ + NH_3$ and $D_2^+ + ND_3$ reactions as measured for the seeded NH_3 and ND_3 samples (a) and for the pure NH_3 and ND_3 samples (c), given as a function of the nominal relative velocity. The experimental data (dots) are scaled by a global factor and compared to the calculated reaction rate coefficients averaged over the measured distributions of rotational states and collision energies $\rho(E_{\mathrm{coll}}; v_f)$ (solid lines) for the seeded samples (b) and for the pure samples (d).

sight, because one would expect dipolar molecules to become less sensitive to the electric field of an ion as their rotational kinetic energy increases. Comparison of the slopes of the $(J, K, |M|, p) = (1, 1, 1, +)$, $(2, 2, 2, +)$, and $(3, 3, 3, +)$ level energies in Fig. 2(d) helps to understand why this is not the case: As J increases, the Stark shifts of these high-field-seeking states become larger, which results in an increase of the rate coefficient that outweighs the contributions from the other Stark states of the same J, K manifolds.

The observed increase of the reaction rate coefficients with increasing rotational excitation of the ammonia molecules appears to contradict the conclusions drawn by Clary for ion-molecule reactions involving ammonia (see Fig. 5 in Ref. [36]). One should note, however, that these calculations were restricted to $K = 0$ rotational levels which do not exhibit the close-to-linear and J-dependent Stark shifts of $|K| > 0$ states (see Fig. 2) that are at the origin of the observed increase of the reaction rate coefficients with increasing rotational excitation. In an earlier article, Clary also reported an increase of the rate coefficients with increasing K value, but the role of the increased rotational excitation remained hidden by the collision-energy dependence (see Fig. 5 in Ref. [35]).

Calculations of the rate coefficients (not shown) indicate a saturation of this effect beyond 50 K, where the reaction rates become almost independent of T_{rot}, while keeping their characteristic collision-energy dependence.

E. Isotope effects on the reaction rate coefficients

Kinetic isotope effects (KIE) upon deuteration are called normal KIE if the ratio of rate coefficients of the undeuterated (k_{H}) to the deuterated samples (k_{D}) $r_{\mathrm{KIE}} = k_{\mathrm{H}}/k_{\mathrm{D}} > 1$ and inverse KIE if $r_{\mathrm{KIE}} = k_{\mathrm{H}}/k_{\mathrm{D}} < 1$. In transition-state theory, normal and inverse KIE are characteristic of "loose" or "tight" transition states, respectively [75,76], but such considerations do not apply for capture-limited reactions, because their rate coefficients are governed by long-range interactions. Figure 8 reveals that the reactions of D_2^+ with NH_3 and ND_3 are subject to a pronounced inverse KIE, which depends both on the

collision energy and on the rotational temperature of the ammonia samples. For the rotationally cold and hot samples, we observe KIEs of $r_{\mathrm{KIE}} = 0.7$ and $r_{\mathrm{KIE}} = 0.5$ at the lowest collision energies, respectively. These large inverse KIEs originate from the different rotational and tunneling energy level structures of NH_3 and ND_3 (see Sec. II B): ND_3 has a higher density of states than NH_3 because of its smaller rotational constant, leading to a larger fraction of the rotational population in states of large J values that have large linear negative Stark shifts. Moreover, the tunneling splitting in ND_3 (0.05 cm^{-1}) is more than one order of magnitude smaller than that in NH_3 (0.8 cm^{-1}). The Stark effect in ND_3 thus becomes linear at smaller electric field strengths, i.e., at larger distances from the D_2^+ ion, leading to higher state-specific rate coefficients [compare Figs. 2(b) and 2(e)]. These two effects make the ND_3-D_2^+ rotationally adiabatic interaction potentials overall more attractive than the NH_3-D_2^+ potentials and explain why the capture rate coefficients of the reactions involving ND_3 are larger than for NH_3.

V. CONCLUSIONS

In this work, we have studied two reactive systems ($D_2^+ + NH_3$ and $D_2^+ + ND_3$) in the gas phase in the collision-energy range from zero to $k_B \times 50$ K for state-selected ions, and for two different rotational temperatures T_{rot} of the neutral molecules, measured by (2 + 1) REMPI spectroscopy. A negative dependence of the reaction rate on the collision energy was observed experimentally for both NH_3 and ND_3 and for both rotational temperatures. These observations could be quantitatively accounted for as arising from the charge-dipole interaction using a rotationally adiabatic capture model. The observed increase of the rate coefficients at decreasing collision energies exactly corresponds to what was observed previously for the He^+ + ammonia reaction [44], as expected for a capture reaction involving ammonia and ions of the same mass.

Our investigation also revealed an increase of the reaction rate coefficients with the rotational temperature, which is counterintuitive in the classical picture of a fast rotating dipole being more difficult to orient in the electric field of an ion. The positive effect of rotational excitation is attributed to the increase, with the rotational angular-momentum quantum number, of the high-field-seeking behavior of ammonia molecules in the field of the ion. The opposite influence of translational and rotational energy on the reaction rate is remarkable and in contrast with the results obtained for other ion-molecule reactions [30,77,78]. The low-field linear Stark shifts (see Fig. 2) are specific of situations where rotational levels of opposite parity are almost degenerate. The observed effect of the rotational temperature is, thus, expected for molecules such as NH_3 and ND_3 as well as diatomic molecules in $\Lambda > 0$ electronic states, an example being the reaction of He^+ and NO [56].

Our study demonstrated a pronounced inverse kinetic isotope effect, the reaction of ND_3 being about twice as fast as for NH_3 at the lowest collision energies and $T_{\mathrm{rot}} \approx 40$ K. The KIE was found to depend on both the collision and rotational energy, which might explain recent discrepancies between measurements of KIEs in ion-molecule reactions [46–48].

The data that support the findings of this study are available from the corresponding author upon reasonable request.

ACKNOWLEDGMENTS

We thank Josef A. Agner and H. Schmutz for their invaluable technical assistance. This work was supported financially by the Swiss National Science Foundation (Project No. 200020B-200478).

[1] R. D. Levine, *Molecular Reaction Dynamics* (Cambridge University Press, Cambridge, England, 2005).
[2] O. Dulieu and A. Osterwalder, *Cold Chemistry: Molecular Scattering and Reactivity near Absolute Zero* (Royal Society of Chemistry, London, 2017), 10.1039/9781782626800.
[3] *State-Selected and State-To-State Ion-Molecule Reaction Dynamics, Part 1. Experiment*, *Advances in Chemical Physics* Vol. 82, edited by C.-Y. Ng, M. Baer, I. Prigogine, and S. A. Rice (Wiley, New York, 1992), 10.1002/9780470141397.
[4] B. R. Heazlewood and T. P. Softley, *Towards chemistry at absolute zero*, Nat. Rev. Chem. **5**, 125 (2021).
[5] Y.-P. Chang, K. Długołęcki, J. Küpper, D. Rösch, D. Wild, and S. Willitsch, *Specific chemical reactivities of spatially separated 3-aminophenol conformers with cold* Ca^+ *ions*, Science **342**, 98 (2013).
[6] P. Puri, M. Mills, I. Simbotin, J. A. Montgomery, R. Côté, C. Schneider, A. G. Suits, and E. R. Hudson, *Reaction blockading in a reaction between an excited atom and a charged molecule at low collision energy*, Nat. Chem. **11**, 615 (2019).
[7] C. R. Markus, O. Asvany, T. Salomon, P. C. Schmid, S. Brünken, F. Lipparini, J. Gauss, and S. Schlemmer, *Vibrational excitation hindering an ion-molecule reaction: The* $c\text{-}C_3H_2^+ - H_2$ *collision complex*, Phys. Rev. Lett. **124**, 233401 (2020).
[8] V. Zhelyazkova, F. B. V. Martins, J. A. Agner, H. Schmutz, and F. Merkt, *Ion-molecule reactions below 1 K: Strong enhancement of the reaction rate of the ion-dipole reaction* $He^+ + CH_3F$, Phys. Rev. Lett. **125**, 263401 (2020).
[9] R. Wild, M. Nötzold, M. Simpson, T. D. Tran, and R. Wester, *Tunnelling measured in a very slow ion-molecule reaction*, Nature (London) **615**, 425 (2023).
[10] E. Herbst and W. Klemperer, *The formation and depletion of molecules in dense interstellar clouds*, Astrophys. J. **185**, 505 (1973).

[11] T. W. Hartquist and A. Dalgarno, *Molecular diagnostics of the interstellar medium and star forming regions*, Astrophys. Space Sci. **237**, 267 (1996).
[12] M. Larsson, W. D. Geppert, and G. Nyman, *Ion chemistry in space*, Rep. Prog. Phys. **75**, 066901 (2012).
[13] I. W. M. Smith, *Laboratory astrochemistry: Gas-phase processes*, Annu. Rev. Astron. Astrophys. **49**, 29 (2011).
[14] M. Jiménez-Redondo, E. Carrasco, V. J. Herrero, and I. Tanarro, *Isotopic exchange processes in cold plasmas of* H_2/D_2 *mixtures*, Phys. Chem. Chem. Phys. **13**, 9655 (2011).
[15] N. Carrasco, C. Alcaraz, O. Dutuit, S. Plessis, R. Thissen, V. Vuitton, R. Yelle, and P. Pernot, *Sensitivity of a Titan ionospheric model to the ion-molecule reaction parameters*, Planet. Space Sci. **56**, 1644 (2008).
[16] J. H. Westlake, J. H. Waite, N. Carrasco, M. Richard, and T. Cravens, *The role of ion-molecule reactions in the growth of heavy ions in Titan's ionosphere*, J. Geophys. Res. Space Phys. **119**, 5951 (2014).
[17] T. Su and W. J. Chesnavich, *Parametrization of the ion-pair molecule collision rate constant by trajectory calculations*, J. Chem. Phys. **76**, 5183 (1982).
[18] D. E. Woon and E. Herbst, *Quantum chemical predictions of the properties of known and postulated neutral interstellar molecules*, Astrophys. J. Suppl. Ser. **185**, 273 (2009).
[19] N. Indriolo, T. Oka, T. R. Geballe, and B. J. McCall, *Constraining the environment of* CH^+ *formation with* CH^+ *observations*, Astrophys. J. **711**, 1338 (2010).
[20] N. G. Adams and D. Smith, *Product-ion distributions for some ion-molecule reactions*, J. Phys. B **9**, 1439 (1976).
[21] D. Smith and N. G. Adams, *The selected ion flow tube (SIFT): Studies of ion-neutral reactions* (Elsevier, New York, 1988), pp. 1–49, 10.1016/S0065-2199(08)60229-8.
[22] J. B. Marquette, B. R. Rowe, G. Dupeyrat, G. Poissant, and C. Rebrion, *Ion-polar-molecule reactions: A CRESU study of* He^+, C^+, $N^+ + H_2O$ *at 27, 68 and 163 K*, Chem. Phys. Lett. **122**, 431 (1985).
[23] A. Potapov, A. Canosa, E. Jiménez, and B. Rowe, *Uniform supersonic chemical reactors: 30 years of astrochemical history and future challenges*, Angew. Chem., Int. Ed. Engl. **56**, 8618 (2017).
[24] L. Biennier, S. Carles, F. Lique, and J. B. Mitchell, *Ion chemistry in uniform supersonic flows*, in *Uniform Supersonic Flows in Chemical Physics* (World Scientific, Singapore, 2022), pp. 173–241, 10.1142/9781800610996_0003.
[25] S. S. Kumar, F. Grussie, Y. V. Suleimanov, H. Guo, and H. Kreckel, *Low temperature rates for key steps of interstellar gas-phase water formation*, Sci. Adv. **4**, eaar3417 (2018).
[26] T. D. Tran, S. Rednyk, A. Kovalenko, Š. Roučka, P. Dohnal, R. Plašil, D. Gerlich, and J. Glosík, *Formation of* H_2O^+ *and* H_3O^+ *cations in reactions of* OH^+ *and* H_2O^+ *with* H_2*: Experimental studies of the reaction rate coefficients from* $T = 15$ *to* 300 *K*, Astrophys. J. **854**, 25 (2018).
[27] S. Venkataramanababu, A. Li, I. O. Antonov, J. B. Dragan, P. R. Stollenwerk, H. Guo, and B. C. Odom, *Enhancing reactivity of* SiO^+ *ions by controlled excitation to extreme rotational states*, Nat. Commun. **14**, 4446 (2023).
[28] S. Willitsch, M. T. Bell, A. D. Gingell, and T. P. Softley, *Chemical applications of laser- and sympathetically-cooled ions in ion traps*, Phys. Chem. Chem. Phys. **10**, 7200 (2008).
[29] O. A. Krohn, K. J. Catani, J. Greenberg, S. P. Sundar, G. da Silva, and H. J. Lewandowski, *Isotope-specific reactions of acetonitrile (*CH_3CN*) with trapped, translationally cold* CCl^+, J. Chem. Phys. **154**, 074305 (2021).
[30] K. Okada, K. Sakimoto, and H. A. Schuessler, *Rotational cooling effect on the rate constant in the* $CH_3F + Ca^+$ *reaction at low collision energies*, J. Phys. Chem. A **126**, 4881 (2022).
[31] A. Voute, A. Dörfler, L. Wiesenfeld, O. Dulieu, F. Gatti, D. Peláez, and S. Willitsch, *Charge transfer of polyatomic molecules in ion-atom hybrid traps: Stereodynamics in the millikelvin regime*, Phys. Rev. Res. **5**, L032021 (2023).
[32] P. Allmendinger, J. Deiglmayr, O. Schullian, K. Höveler, J. A. Agner, H. Schmutz, and F. Merkt, *New method to study ion-molecule reactions at low temperatures and application to the* $H_2^+ + H_2 \rightarrow H_3^+ + H$ *reaction*, ChemPhysChem **17**, 3596 (2016).
[33] A. G. Harrison and J. C. J. Thynne, *Concurrent ion-molecule reactions. Part 4.—Reactions in mixtures of ammonia and water with deuterium and methane*, Trans. Faraday Soc. **64**, 945 (1968).
[34] J. K. Kim and W. T. Huntress, *Ion cyclotron resonance studies on the reaction of* H_2^+ *and* D_2^+ *ions with various simple molecules and hydrocarbons*, J. Chem. Phys. **62**, 2820 (1975).
[35] D. C. Clary, *Rate constants for the reactions of ions with dipolar polyatomic molecules*, J. Chem. Soc., Faraday Trans. 2 **83**, 139 (1987).
[36] D. C. Clary, *Fast chemical reactions: Theory challenges experiment*, Annu. Rev. Phys. Chem. **41**, 61 (1990).
[37] F. B. V. Martins, V. Zhelyazkova, Ch. Seiler, and F. Merkt, *Cold ion chemistry within a Rydberg-electron orbit: Test of the spectator role of the Rydberg electron in the* $He(n) + CO \rightarrow C(n') + O + He$ *reaction*, New J. Phys. **23**, 095011 (2021).
[38] *Rydberg States of Atoms and Molecules*, edited by R. F. Stebbings and F. B. Dunning (Cambridge University Press, Cambridge, England, 1983).
[39] S. T. Pratt, J. L. Dehmer, P. M. Dehmer, and W. A. Chupka, *Reactions of Rydberg states of molecular hydrogen*, J. Chem. Phys. **101**, 882 (1994).
[40] E. Wrede, L. Schnieder, K. Seekamp-Schnieder, B. Niederjohann, and K. H. Welge, *Reactive scattering of Rydberg atoms:* $H^* + D_2 \rightarrow HD + D^*$, Phys. Chem. Chem. Phys. **7**, 1577 (2005).
[41] M. Matsuzawa, *Highly excited Rydberg electron as a spectator to an ion-molecule reaction*, Phys. Rev. A **82**, 054701 (2010).
[42] R. A. Dressler, Y. Chiu, D. J. Levandier, X. N. Tang, Y. Hou, C. Chang, C. Houchins, H. Xu, and C.-Y. Ng, *The study of state-selected ion-molecule reactions using the vacuum ultraviolet pulsed field ionization-photoion technique*, J. Chem. Phys. **125**, 132306 (2006).
[43] M. Malow, K. Brembs, and K.-M. Weitzel, *Ion-molecule reactions of state selected* HCl^+ *ions with carbon dioxide and ethene*, Z. Phys. Chem. **215**, 737 (2001).
[44] V. Zhelyazkova, F. B. V. Martins, J. A. Agner, H. Schmutz, and F. Merkt, *Multipole-moment effects in ion-molecule reactions at low temperatures: Part I—Ion-dipole enhancement of the rate coefficients of the* $He^+ + NH_3$ *and*

$He^+ + ND_3$ *reactions at collisional energies* E_{coll}/k_B *near 0 K*, Phys. Chem. Chem. Phys. **23**, 21606 (2021).

[45] L. S. Petralia, A. Tsikritea, J. Loreau, T. P. Softley, and B. R. Heazlewood, *Strong inverse kinetic isotope effect observed in ammonia charge exchange reactions*, Nat. Commun. **11**, 173 (2020).

[46] A. Tsikritea, K. Park, P. Bertier, J. Loreau, T. P. Softley, and B. R. Heazlewood, *Inverse kinetic isotope effects in the charge transfer reactions of ammonia with rare gas ions*, Chem. Sci. **12**, 10005 (2021).

[47] S. G. Ard, A. A. Viggiano, B. C. Sweeny, B. Long, and N. S. Shuman, *Inconsistent kinetic isotope effect in ammonia charge exchange reaction measured in a Coulomb crystal and in a selected-ion flow tube*, Nat. Commun. **13**, 3310 (2022).

[48] L. S. Petralia, A. Tsikritea, J. Loreau, T. P. Softley, and B. R. Heazlewood, *Reply to: Inconsistent kinetic isotope effect in ammonia charge exchange reaction measured in a Coulomb crystal and in a selected-ion flow tube*, Nat. Commun. **13**, 3311 (2022).

[49] J. Toscano, H. J. Lewandowski, and B. R. Heazlewood, *Cold and controlled chemical reaction dynamics*, Phys. Chem. Chem. Phys. **22**, 9180 (2020).

[50] F. Merkt, *Molecular-physics aspects of cold chemistry*, in *Current Trends in Atomic Physics, Les Houches 2016 Lecture Notes*, edited by A. Browaeys, T. Lahaye, T. Porto, C. S. Adams, M. Weidemüller, and L. F. Cugliandolo (Oxford University Press, New York, 2019), pp. 82–141, 10.1093/oso/9780198837190.003.0003.

[51] P. Langevin, *Une formule fondamentale de théorie cinétique*, Ann. Chim. Phys. T **5**, 245 (1905).

[52] T. Su and M. T. Bowers, *Parameterization of the average dipole orientation theory: Temperature dependence*, Int. J. Mass Spectrom. Ion Phys. **17**, 211 (1975).

[53] D. C. Clary, D. Smith, and N. G. Adams, *Temperature dependence of rate coefficients for reactions of ions with dipolar molecules*, Chem. Phys. Lett. **119**, 320 (1985).

[54] D. C. Clary, *Calculations of rate constants for ion-molecule reactions using a combined capture and centrifugal sudden approximation*, Mol. Phys. **54**, 605 (1985).

[55] J. Troe, *Statistical adiabatic channel model for ion molecule capture processes*, J. Chem. Phys. **87**, 2773 (1987).

[56] V. Zhelyazkova, F. B. V. Martins, S. Schilling, and F. Merkt, *Reaction of an ion and a free radical near 0 K:* $He^+ + NO \rightarrow He + N^+ + O$, J. Phys. Chem. A **127**, 1458 (2023).

[57] G. Wichmann, E. Miloglyadov, G. Seyfang, and M. Quack, *Nuclear spin symmetry conservation studied by cavity ring-down spectroscopy of ammonia in a seeded supersonic jet from a pulsed slit nozzle*, Mol. Phys. **118**, e1752946 (2020).

[58] K. Höveler, J. Deiglmayr, J. A. Agner, H. Schmutz, and F. Merkt, *The* $H_2^+ + HD$ *reaction at low collision energies:* H_3^+/H_2D^+ *branching ratio and product-kinetic-energy distributions*, Phys. Chem. Chem. Phys. **23**, 2676 (2021).

[59] H. Shinohara, *Two-photon-ionization mass spectroscopy of ammonia clusters in a pulsed supersonic nozzle beam*, J. Chem. Phys. **79**, 1732 (1983).

[60] Y. Shagam and E. Narevicius, *Sub-Kelvin collision temperatures in merged neutral beams by correlation in phase-space*, J. Phys. Chem. C **117**, 22454 (2013).

[61] J. Jankunas, B. Bertsche, and A. Osterwalder, *Study of the* $Ne(^3P_2) + CH_3F$ *electron-transfer reaction below 1 K*, J. Phys. Chem. A **118**, 3875 (2014).

[62] C. Menzel, A. Knöner, J. Kutzner, and H. Zacharias, *Scattering of neutral* NH_3 *clusters off* LiF(100)*: Angular distributions of* NH_3 *and small clusters*, Z. Phys. D **38**, 179 (1996).

[63] W. G. Gang, E. J. Kim, C. J. Choe, G. U. Jeong, and G. H. Jeong, *Time resolved molecular beam characteristic in a pulsed supersonic jet*, Bull. Korean Chem. Soc. **16**, 238 (1995).

[64] V. M. Torres, R. B. Doak, B. J. Wilkens, D. J. Smith, and I. S. T. Tsong, *Selected energy epitaxial deposition of* GaN *and* AlN *on* SiC(0001) *using seeded supersonic free jets of* NH_3 *in helium*, J. Vac. Sci. Technol. A **17**, 1570 (1999).

[65] C. Bobbert, S. Schütte, C. Steinbach, and U. Buck, *Fragmentation and reliable size distributions of large ammonia and water clusters*, Eur. Phys. J. D **19**, 183 (2002).

[66] H. Dickinson, D. Rolland, and T. P. Softley, *Multichannel quantum defect theory (MQDT) analysis of the* $(2 + 1')$ *mass analyzed threshold ionization (MATI) spectroscopy of* NH_3, J. Phys. Chem. A **105**, 5590 (2001).

[67] C. M. Western, PGOPHER*: A program for simulating rotational, vibrational and electronic spectra*, J. Quant. Spectrosc. Radiat. Transfer **186**, 221 (2017).

[68] L. Fusina, G. di Lonardo, and J. Johns, *Inversion-rotation spectrum and spectroscopic parameters of* $^{14}ND_3$ *in the ground state*, J. Mol. Spectrosc. **112**, 211 (1985).

[69] P. Chen, J. Pearson, H. M. Pickett, S. Matsuura, and G. A. Blake, *Measurements of* $^{14}NH_3$ *in the* $\nu_2 = 1$ *state by a solid-state, photomixing, THz spectrometer, and a simultaneous analysis of the microwave, terahertz, and infrared transitions between the ground and* ν_2 *inversion-rotation levels*, J. Mol. Spectrosc. **236**, 116 (2006).

[70] J. Bentley, B. Cotterell, A. Langham, and R. Stickland, $2 + 1$ *resonance-enhanced multiphoton ionisation spectroscopy of the high* ν_2 *levels of the* $\tilde{B}\ ^1E''$ *Rydberg state of* NH_3 *(*ND_3*)*, Chem. Phys. Lett. **332**, 85 (2000).

[71] M. Nolde, K.-M. Weitzel, and C. M. Western, *The resonance enhanced multiphoton ionisation spectroscopy of ammonia isotopomers* NH_3, NH_2D, NHD_2 *and* ND_3, Phys. Chem. Chem. Phys. **7**, 1527 (2005).

[72] J. H. Glownia, S. J. Riley, S. D. Colson, and G. C. Nieman, *MPI spectroscopy of expansion-cooled ammonia: Structure and dynamics at 50 K*, J. Chem. Phys. **72**, 5998 (1980).

[73] M. Scotoni, M. Zen, D. Bassi, A. Boschetti, and M. Ebben, *An opto-thermal study of* NH_3 *rotational relaxation in* $NH_3 - He$ *supersonic expansions*, Chem. Phys. Lett. **155**, 233 (1989).

[74] D. L. Snavely, S. D. Colson, and K. B. Wiberg, *Rotational cooling in a supersonic expansion of ammonia*, J. Chem. Phys. **74**, 6975 (1981).

[75] S. S. Glad and F. Jensen, *Transition state looseness and α-secondary kinetic isotope effects*, J. Am. Chem. Soc. **119**, 227 (1997).

[76] Y.-F. Chen, Y.-T. Tsai, L. Hirsch, and D. M. Bassani, *Kinetic isotope effects provide experimental evidence for proton tunneling in methylammonium lead triiodide perovskites*, J. Am. Chem. Soc. **139**, 16359 (2017).

[77] A. A. Viggiano, J. M. Van Doren, R. A. Morris, and J. F. Paulson, *Evidence for an influence of rotational energy on the rate constants for the reaction of* Ar^+ *(*$^2P_{3/2}$*) with* N_2, J. Chem. Phys. **93**, 4761 (1990).

[78] L. S. Sunderlin and P. B. Armentrout, *Rotational temperature dependence of the reactions of* N^+ *and* C^+ *with* H_2, HD, *and* D_2, J. Chem. Phys. **100**, 5639 (1994).